

# Towards Flexible Wireless Charging for Medical Implants Using Distributed Antenna System

Xiaoran Fan<sup>\*,†</sup>, Longfei Shangguan<sup>‡</sup>, Richard Howard<sup>†</sup>, Yanyong Zhang<sup>\*</sup>  
Yao Peng<sup>\*</sup>, Jie Xiong<sup>◊</sup>, Yunfei Ma<sup>×</sup>, Xiang-Yang Li<sup>\*</sup>

<sup>\*</sup>University of Science and Technology of China, <sup>†</sup>Rutgers University, <sup>‡</sup>Microsoft  
<sup>\*</sup>Northwest University, <sup>◊</sup>UMASS Amherst, <sup>×</sup>Alibaba Group

## ABSTRACT

This paper presents the design, implementation and evaluation of In-N-Out, a software-hardware solution for far-field wireless power transfer. In-N-Out can continuously charge a medical implant residing in deep tissues at near-optimal beamforming power, even when the implant moves around inside the human body. To accomplish this, we exploit the unique energy ball pattern of distributed antenna array and devise a backscatter-assisted beamforming algorithm that can concentrate RF energy on a tiny spot surrounding the medical implant. Meanwhile, the power levels on other body parts stay in low level, reducing the risk of overheating. We prototype In-N-Out on 21 software-defined radios and a printed circuit board (PCB). Extensive experiments demonstrate that In-N-Out achieves 0.37 mW average charging power inside a 10 cm-thick pork belly, which is sufficient to wirelessly power a range of commercial medical devices. Our head-to-head comparison with the state-of-the-art approach shows that In-N-Out achieves  $5.4\times$ – $18.1\times$  power gain when the implant is stationary, and  $5.3\times$ – $7.4\times$  power gain when the implant is in motion.

## CCS CONCEPTS

• **Hardware** → **Wireless devices; Bio-embedded electronics; Platform power issues**; • **Networks** → *Wireless access points, base stations and infrastructure.*

## KEYWORDS

Backscatter, Wireless Charging, Medical Implants, Distributed Beamforming

## ACM Reference Format:

Xiaoran Fan<sup>\*,†</sup>, Longfei Shangguan<sup>‡</sup>, Richard Howard<sup>†</sup>, Yanyong Zhang<sup>\*</sup> and Yao Peng<sup>\*</sup>, Jie Xiong<sup>◊</sup>, Yunfei Ma<sup>×</sup>, Xiang-Yang Li<sup>\*</sup>. 2020. Towards Flexible Wireless Charging for Medical Implants Using Distributed Antenna System. In *The 26th Annual International Conference on Mobile Computing and Networking (MobiCom '20)*, September 21–25, 2020, London, United Kingdom. ACM, New York, NY, USA, 15 pages. <https://doi.org/10.1145/3372224.3380899>

Permission to make digital or hard copies of all or part of this work for personal or classroom use is granted without fee provided that copies are not made or distributed for profit or commercial advantage and that copies bear this notice and the full citation on the first page. Copyrights for components of this work owned by others than ACM must be honored. Abstracting with credit is permitted. To copy otherwise, or republish, to post on servers or to redistribute to lists, requires prior specific permission and/or a fee. Request permissions from [permissions@acm.org](mailto:permissions@acm.org).

*MobiCom '20, September 21–25, 2020, London, United Kingdom*

© 2020 Association for Computing Machinery.

ACM ISBN 978-1-4503-7085-1/20/09...\$15.00

<https://doi.org/10.1145/3372224.3380899>

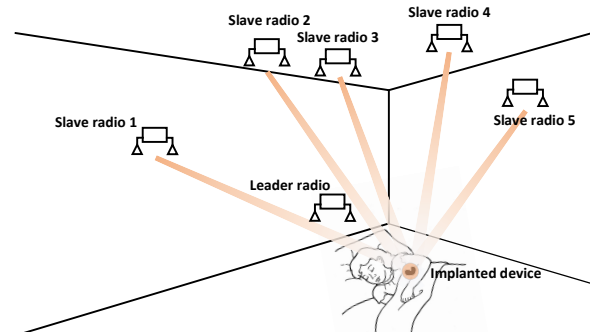


**Figure 1: An illustration of In-N-Out deployment. The leader radio coordinates multiple slave radios to charge the pacemaker during bedtime.**

## 1 INTRODUCTION

Each year millions of patients improve their quality of life through medical implants [67]. These devices are inserted into the human body to replace a missing body part [24], modify a body function [3], or provide supports to organs and tissues [28]. While functional innovations on medical implants are going full steam ahead, the amount of energy required by these devices remains substantial. Though cutting-edge batteries could enable medical implants (*e.g.*, pacemaker [23]) to function for years [2, 94], the use of battery is not always feasible – there may not be enough space inside the brain or body as a battery’s size is proportional to its lifetime [36]. We have thus seen cumbersome solutions such as placing the battery of a brain stimulator in the user’s chest or even outside the body, with wires running between the battery and the stimulator. Battery replacement, on the other hand, is risky as it usually requires a surgery that may introduce extra complications [5, 52].

Wireless charging has received attention in recent years as a viable alternative. The concept of wireless charging, however, is not new. From early 1900s Tesla’s Wardenclyffe tower [30] to the later Air Force mission of powering an unmanned helicopter [39], wireless charging has witnessed significant breakthroughs over the past century. Today wireless charging can be simply performed on an office desk or in a car. As far as medical implants are concerned, they are primarily charged through electromagnetic coupling in the near field [43, 64, 74, 92, 97]. These near-field charging systems use dedicated coils that usually require contact with human tissues. A critical drawback of these systems is that their charging efficiency drops significantly with the reduction of coil size and the increase of coil separation, which severely hinders the miniaturization of medical implants [59]. Another drawback of these near-field systems is

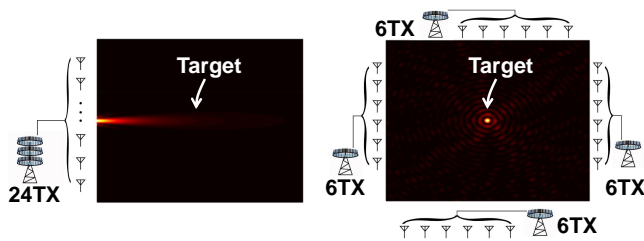


**Figure 2: The energy heatmap produced by (left) a linear 24-antenna array and (right) a distributed 24-antenna array. The linear antenna array produces an energy beam spreading in the direction of the target, while the distributed antenna array produces an energy spot surrounding the target.**

the low flexibility: the users are required to wear bulky transmitter coils and carefully align them with the implant coils [10]. Even though the user can stay static for hours, the inter-coil coupling can be easily broken as the implant coils may move as blood flows [18]. Thus, a contactless means of wireless charging holds appeal as a flexible and less invasive alternative.

This paper presents In-N-Out, a flexible far field power transfer system that owns two desirable properties: 1) it does not require the user to wear cumbersome charging devices. 2) it can continuously charge the medical implant residing in deep tissues with consistently near-optimal power, even when the implant moves around inside the human body. To do so, In-N-Out leverages *beamforming* to combine signals coherently at the medical implant. At the heart of beamforming is the accurate measurement of channel state information (CSI) of each wireless channel. This is usually achieved by having the transmitter send a preamble, where the receiver (e.g., a medical implant) uses this preamble to estimate the CSI of the forward channel. This CSI value is then fed back for transmitter beamforming.

However, CSI measurement becomes very challenging, if at all possible, for medical implants. RF signal generation is power hungry, which becomes especially challenging for medical implants that are deeply power constrained [59]. In practice, to minimize power consumption, the RF radio of a medical implant typically adopts a rather low power amplification coefficient [56]. Therefore, the resulting preamble signals are very weak, which are made even worse by the fast decaying radiation efficiency of an in-body antenna. The antenna’s radiation efficiency decays significantly due to its miniature size, i.e., 10 – 20 dB loss compared to the weak transmission signals [70, 100]. Furthermore, RF signals experience exponentially more attenuation in human tissues than in air, e.g., 40 dB loss over just a few centimeters in muscles [44]. As a result, the received signal is usually well below the noise floor, hence the failure to provide accurate CSI estimation.

To solve these challenges, the state-of-the-art, IVN [77], proposes to encode the frequency of multiple transmission signals in hopes of these frequency-varying signals coherently combine at the medical implant from time to time, without CSI measurements. IVN achieves high beamforming power intermittently to cold start the medical implant. It is, however, ill-suited for power transfer as the beamforming power it actually produces, for most

of the time, is far less than the *maximal* beamforming power.<sup>1</sup> The coherent-incoherent beamforming nature renders the power delivery particularly inefficient.

In In-N-Out, we devise a coherent beamforming algorithm that can continuously achieve the maximal beamforming power at the medical implant, even when the implant moves around inside the human body. Our algorithm builds upon the iterative one-bit phase alignment approach proposed in [84, 85], which involves the receiver sending a feedback signal to describe the received beamforming power change after each iteration until reaching the maximal. Though this approach can accomplish consistently coherent beamforming, it cannot be directly adopted in our setting because frequently measuring beamforming power and sending feedback signals would even consume more power than what can be wirelessly harvested at the implant. Thus, leveraging the one-bit phase alignment approach as a generic framework, we take into consideration the unique challenges in our scenario and design a backscatter assisted beamforming (in short, BAB) scheme. Our BAB scheme employs a customized monotonic *backscatter* radio at the implant that simply reflects signals and another nearby auxiliary radio that assesses the received backscatter signal power change. In this way we successfully offload power-consuming operations at the medical implant (e.g., power assessment, signal generation and transmission) to the auxiliary radio outside human body, and thus significantly cut down the energy consumption compared to existing systems where implant radios have to directly assess the received power change and produce feedback signals.

However, new challenges arise when we use backscatter radios at the implants. After going through excessive channel fading in both directions, the received backscatter signal is usually well below the noise floor, hence causing the new challenge of detecting/decoding the weak backscatter signal. In-N-Out addresses this challenge by pre-coding the carrier signal using chirp spreading spectrum (CSS) modulation. The frequency-domain processing gain of CSS enables In-N-Out to detect the backscatter signal even 35dB<sup>2</sup> below the noise floor.

We prototype In-N-Out on 21 USRP software defined radios and evaluate its performance in various settings. In our prototype, we adopt distributed antenna layout that addresses the safety concerns of wireless charging. Performing beamforming using co-located antennas will generate a high energy beam along a specific angle, as shown in Figure 2(left). This high energy beam does not only cover the medical implant but also part of the human body, likely resulting in excessive heating of human tissues. In contrast, beamforming with distributed antennas produces a tiny energy spot surrounding the target location as shown in Figure 2(right) and the energy density at other locations is significantly lower due to destructive interference [46–49]. Therefore, it naturally avoids overheating other areas of the body while charging the target. Moreover, these distributed antennas have different orientations and are thus insensitive to the orientation of the implant.

Our field studies show that In-N-Out’s beamforming algorithm is efficient (< 0.3 s latency) and reliable (insensitive to the implant’s

<sup>1</sup>Defined as the power level measured at the target location when all wireless transmissions are coherently combined.

<sup>2</sup>In-N-Out does not need to decode the packet but detect the power change of backscatter signals.

rotation and motion). It achieves 0.37 mW charging power on average when the implant is 2 m away, which is sufficient to power a range of medical devices from outside the body. Our head-to-head comparison with IVN [77] shows that In-N-Out achieves  $5.4\times$ – $18.1\times$  and  $5.3\times$ – $7.4\times$  average power gain over IVN in stationary and low-speed mobile scenarios, respectively.

In-N-Out's contributions include:

- Designing a software-hardware solution for deep tissue power transfer. We devise a set of signal processing algorithms and a low-power, monotonic backscatter radio that enables In-N-Out to charge the medical implant at the maximal beamforming power, even when the implant moves around inside the human body. Our system consists of several technical innovations, including backscatter-leader-slave three-party beamforming without explicit CSI measurement, two-phase leader-slave chirp synchronization design, radio cold start through intentionally imperfect phase alignment, *etc.*
- Prototyping the system on software-defined radios and a PCB board, and conducting comprehensive evaluation of the system. Our evaluation takes into consideration the impact of important parameters such as the charging medium, system size, chirp bandwidth, antenna array size, *etc.* We also conduct head-to-head comparisons with the state-of-the-art approach in a range of settings.

In the next section (§2), we introduce the scope of our work. We introduce beamforming primer in Section 3. The system design is detailed in Section 4. An implementation (§5) and performance evaluation (§6) then follow. Section 7 summarizes related works. We discuss future works in Section 8 and conclude the work in Section 9.

## 2 SCOPE

This work aims to developing a practical wireless charging system, with the hope of extending the lifetime of medical implants.

The lifetime of a medical implant depends mainly on the lifetime of its battery [8]. Hence a lot of efforts have been made to improve the battery life [81], either by increasing the battery capacity or minimizing the device power consumption. Today state-of-the-art pacemakers can last for over ten years [27]. However, the user still needs a surgery for replacement when the battery is depleted. To lengthen the implant's lifetime, In-N-Out can serve as a supplementary power supply – whenever the user stays in a space where a personalized In-N-Out system is available, the implant can be charged, without drawing power from the regular battery. As a result, the lifetime of the implant can be significantly extended.

We note that though In-N-Out is primarily designed for wireless power transfer, its application scope can be much broader. For example, In-N-Out could potentially serve as a communication system to collect the biomedical data from inbody sensors [40, 72]. Compared with conventional gastroscopy that requires the patient to swallow a tube for data collection [17], our solution is much less invasive.

**Possible Deployment Scenarios.** We envision the In-N-Out system will be deployed in the user's personal space (home and/or office). Given a typical bedroom ( $4\times 4\text{ m}^2$  rectangular area with a 2.8 m average target-antenna distance), if we keep the number

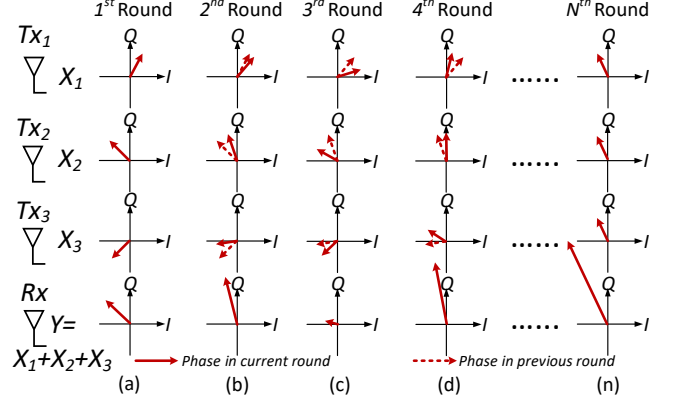


**Figure 3: A running example of the one-bit phase alignment algorithm with three transmitters. Each transmitter adjusts its phase based on the feedback from the receiver and gradually converges to the optimal phase alignment.**

of radios to a reasonable number, i.e., less than 14 (each emitting 30 dBm signals), then the resulting power density at any location in the room is well below the power limit specified by FCC regulation ( $0.6\text{ mw/cm}^2$  [1]).

## 3 BEAMFORMING WITHOUT CSI FEEDBACK

Due to excessive channel fading and inhomogeneous channel propagation in deep tissues, CSI measurement becomes very challenging, if at all possible, for medical implants embedded in deep tissues (will be explained in §4.1.1). Instead of pursuing a precise CSI measurement, we employ a non-CSI beamforming approach proposed in [84, 85], referred as one-bit phase alignment algorithm.

**Algorithm overview.** The one-bit phase alignment algorithm goes through multiple rounds and then converges to the optimal phase settings. In each round, each transmitter updates the phase of the transmission signal based on the feedback sent from the receiver. The phase value in the current round is randomly selected within the range of  $\pm\Phi$  with respect to the phase value in the previous round (we discuss the optimal  $\Phi$  setting in §4.3). Phase update can be formulated as follows:

$$\theta_i(n+1) = \begin{cases} \theta_i(n) + \delta_i(n), & \text{if } y[n] > y[n-1], -\Phi \leq \delta_i(n) \leq \Phi, \\ \theta_i(n-1) + \delta_i(n), & \text{otherwise,} \end{cases}$$

where  $\theta_i(n)$  is the phase setting of the  $i^{\text{th}}$  transmitter in the  $n^{\text{th}}$  round and  $y[n]$  is the received signal power in the  $n^{\text{th}}$  round.

**An example.** We use a simple example scenario involving three transmitters to explain this algorithm. In the first round, each transmitter randomly chooses a phase value, as shown in Figure 3(a). The receiver records beamforming power. In the second round, each transmitter randomly chooses a phase that is within the range of  $\pm\Phi$  from its phase value in the first round. This new phase leads to an increased beamforming power, as shown in Figure 3(b). The receiver notifies transmitters this power increase (†) with a single bit feedback. Hence in the third round, each transmitter uses its round two phase value as the reference and updates its phase accordingly, which unfortunately leads to a degraded beamforming power (‡), shown in Figure 3(c). Therefore, in the fourth round,

each transmitter again uses its round two phase value as the reference (Figure 3(d)). The algorithm iterates in the fashion until the beamforming power reaches its maximum (Figure 3(n)).

## 4 SYSTEM DESIGN

In-N-Out involves a *leader* radio and several *slave* radios working on 915 MHz ISM band,<sup>3</sup> as shown in Figure 1. The leader node detects and decodes feedback signals sent from the medical implant and uses decoded information to govern the phase alignment of slaves in the next round. As the medical implant may move around while charging, we do not assume any prior knowledge of the implant's location. To minimize the energy consumption due to feedback signal creation and transmission, we design a low-power backscatter radio that offloads the computation from the medical implant to the leader radio that is outside of the human body (§4.1). As a proof of concept, we use a dedicated radio (*i.e.* USRP) as the leader radio. However, we envision the leader radio can simply be a smartphone being able to talk with slave radios wirelessly (*e.g.*, through Wi-Fi).

In the rest of this section, we explain the details of each design component, including carrier signal design and synchronization (§4.1.1), low-power backscatter radio design (§4.1.2), and power change inference algorithm (§4.1.3). Finally, we explain the way to bootstrap the system during the cold start in §4.2 and discuss the way to balance beamforming convergence and delay in §4.3.

### 4.1 Backscatter Assisted Beamforming (BAB)

Directly applying one-bit phase alignment algorithm to in-body wireless charging is unfeasible due to its excessive energy overhead. Generating a feedback signal with even the simplest modulation scheme (*i.e.* frequency shift keying (FSK)) costs at least tens of milliwatts [60], which can quickly add up when we go through each iteration. This operation alone would consume more power than what can be wirelessly delivered to the implant. To address this dilemma, we replace the default active radio on the medical implant with a low-power backscatter radio. A backscatter radio, while being able to minimize the implant's power consumption, raises new challenges and complicates the system design nonetheless. Below we discuss these challenges in detail as well as our solutions.

**4.1.1 Carrier Signal.** Backscatter radio neither generates carrier signals nor amplifies transmission signals. It instead modulates data on top of the ambient carrier signal (a sinusoidal tone coming from a nearby active radio) and reflects the modulated signal (termed as backscatter signal) back to the receiver. Compared with the active radio, the backscatter radio saves three to four orders of magnitude transmission power by avoiding power consumption on carrier generator and power amplifier [102]. However, the lack of power amplifier renders the backscatter signal extremely weak, which is then made much worse by the excessive fading in deep tissues. Table 1 shows the break-down signal attenuation as the carrier signal goes through the human body and reflected by the backscatter radio. The receiving power is around -128 dBm on average, well below the ambient RF noise floor measured by an USRP

<sup>3</sup>Working on 2.4 Ghz or 5 Ghz ISM band may introduce severe interference to ongoing Wi-Fi traffic, whereas working on lower ISM band (*i.e.* 433 MHz) requires a bulky receiving antenna which is not suited for implant devices.

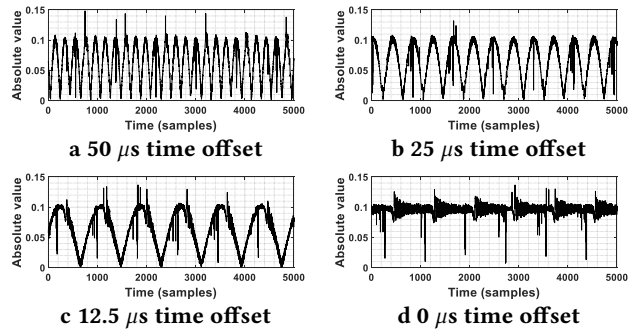


**Figure 4: RSS measurements in different time offset settings. A larger time offset leads to a higher RSS fluctuation rate. The RSS converges to a relatively stable value when all chirps are tightly time synchronized.**

N210 in the same frequency band.<sup>4</sup> Hence, both CSI and RSS measurement are unreliable for channel estimation (CSI measurement at 915MHz band requires at least 6 dB higher signal strength than RSS measurement [57]).

An intuitive approach is to have the backscatter radio leverage more advanced coding mechanisms to improve the signal to noise ratio (SNR) of the backscatter signal. However, this requires more complicated, power hungry analog-to-digital (ADC) and digital circuits and will again complicate the implant radio design and boost the overall energy consumption.

To minimize the power consumption of the backscatter radio, we offload most of its operations to the radios outside the human body. Taking a step further, we adopt chirp spread spectrum (CSS) – a chirp pulse modulation that linearly sweeps a frequency band to generate the carrier signal – to further cut down the power consumption. Compared with conventional sinusoidal tone, CSS enables the wireless signal to be decodable below the noise floor (*e.g.*, -137dBm for LoRa [9]) by introducing the unique processing gain on the frequency domain. Given a fixed transmission power, the processing gain ( $PG$ ) is proportional to the product of the chirp symbol time  $S_t$  and the bandwidth  $S_{bw}$ :  $PG \propto S_t \times S_{bw}$  [86]. We can thus have different trade-offs between system delay and spectrum utilization in different scenarios, without hurting the signal detection accuracy. In the following examples, we set the chirp bandwidth and symbol time to 40 KHz and 4 ms. We have also explored other settings in our evaluation (§6.1.3).

**Chirp synchronization.** Tight time synchronization of chirp signals is the key to the success of beamforming. Otherwise the beamforming power will fluctuate drastically due to the periodical coherent and incoherent signal combinations. We design a *two-step chirp synchronization algorithm* for this purpose. In the first step, the leader radio broadcasts a chirp preamble. The slave radio synchronizes with this preamble through cross-correlation. The resulting lag then translates into a sample offset between the reference chirp and the received chirp preamble. Each slave radio can thus compensate for this initial time offset. However, due to heterogeneous software and hardware processing delays among radios, residual time offset still remains.

<sup>4</sup>-70 dBm on 915 MHz frequency band measured in an office building.

Tx power (dBm)	Air path loss (dBm) dist. (1 – 10m)	Skin reflection /absorption (dBm)	Muscle path loss (dBm) dist. (2 – 6cm)	Insertion loss (dBm)	Muscle path loss (dBm) dist. (2 – 6cm)	Skin reflection /absorption (dBm)	Air path loss (dBm) dist. (1 – 10m)	Rx power (dBm)
30 [1]	31.67 – 51.67 [104]	3[93]	9.2 – 27.6 [69, 99]	30 [109]	9.2 – 27.6 [69, 99]	5[93]	31.67 – 51.67 [104]	-89.74 – -166.54

**Table 1: The power loss at different part of the round-trip path between the transmitter (outside body) and the receiver (inside body). The transmission power is set to the maximum value under FCC regulation.**

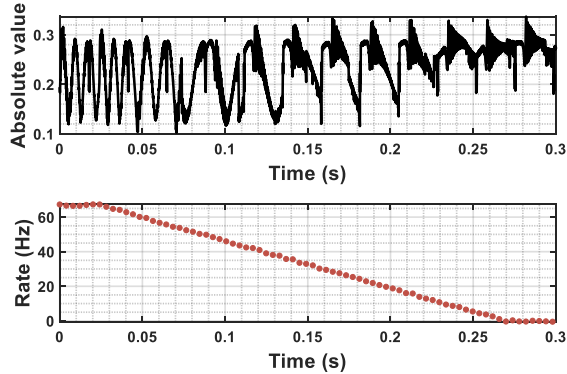


**Figure 5: A snapshot of RSS samples (top) and the fluctuation rate (bottom) in one period. The fluctuation rate decreases with time. The signal amplitude converges when the two radios are synchronized.**

In the second step, the slave radios transmit a continuous chirp signal; the leader radio listens. All slave radios then take turns to compensate for the residual time offset under the guidance of the leader radio. This is based on the realization that the amplitude of the superimposed signal (at the leader radio) will fluctuate periodically if the incoming chirps are not tightly time synchronized. In fact, the larger the time offset, the faster the received signal amplitude fluctuates, as shown in Figure 4. The leader radio computes the fluctuation rate of the received signal amplitude using fast Fourier transform (FFT) and then guides slave radios to compensate for the residual time offset.

The second step goes through a total of  $N - 1$  periods. In each period  $i$ , In-N-Out aligns the initial time of the  $i + 1^{th}$  slave to the first slave. Specifically, in the first period, two slave radios  $S_1$  and  $S_2$  send a continuous chirp signal simultaneously. These two signals add up at the leader radio. Since  $S_1$  and  $S_2$  are not strictly time synchronized, we will see fluctuations of the received signal at the leader radio. The leader then sends a two-bit feedback to  $S_2$ , telling this node to add or subtract one sample time, or to stop.  $S_2$  calibrates its clock based on this feedback, and then regenerate a chirp signal with an updated clock. The leader radio detects the change of the fluctuation rate and sends an updated feedback to  $S_2$ . The algorithm iterates as above until all slave radios are synchronized. The algorithm then enters the next period and involves one more slave radio. All slaves are tightly time synchronized at the end of the last period.

Considering its iterative nature, one may fear our synchronization algorithm may cause an excessively long delay. However, the first step of the algorithm can already yield small residual time offset and usually a reasonable number of iterations (tens) are needed in each period. Figure 5 shows the variation of received signals (top)

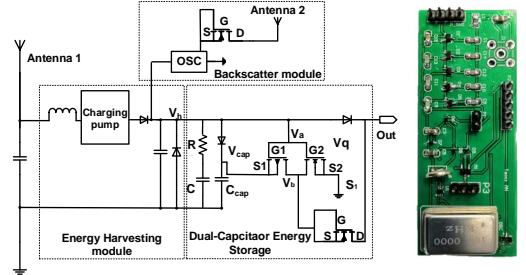


**Figure 6: Our monotonic backscatter radio design (left) and the PCB board prototype (right). We envision the board size can be reduced to the sub-centimeter scale when implementing In-N-Out on an Integrated Circuit (IC).**

and the fluctuation rate (bottom) in one period. The fluctuation rate drops to almost zero in 0.27 s.

**4.1.2 Backscatter Design.** The chirp modulation enables the leader radio to detect the weak backscatter signal. However, generating this backscatter signal requires the backscatter radio to measure the received power and compare it with the signal power measured in previous round. These operations require extra hardware, computation and more importantly, power consumption.

To solve this challenge, we offload power measurement from the backscatter radio to the leader radio outside human body. We choose this design based on the key observation of the monotonic backscatter system: the backscatter signal power changes monotonically with the received beamforming power. By observing the power change of the received backscatter signals, the leader radio could infer the power change of the received beamforming power.

In In-N-Out, the backscatter radio shifts the superimposed carrier signal to another frequency band (for interference avoidance) and reflects it directly back to the leader radio. This is achieved by letting the backscatter radio generate a baseband signal at frequency  $f_s$  and mix this baseband with the superimposed carrier signal at frequency  $f_1$ . The mixer operation will shift this superimposed carrier signal to another two frequency bands:  $f_1 + f_s$  and  $f_1 - f_s$ . The leader radio detects the backscatter signal on one of these two frequency bands and infers the beamforming power change accordingly. Following the iterative beamforming algorithm introduced in §3, the leader radio then guides slave radios to adjust their signal phase settings. To avoid interference between the carrier signal and the backscatter signal, we conservatively set  $f_s$  to 100 KHz, which is  $1.5\times$  larger than the default chirp bandwidth (40 KHz).

**Radio hardware design.** Conventional backscatter design (e.g., RFID), however, is not always monotonic, as shown in Figure 7(top). This non-monotonic property arises from the energy harvesting circuit where the impedance of matching network changes with input RF power.

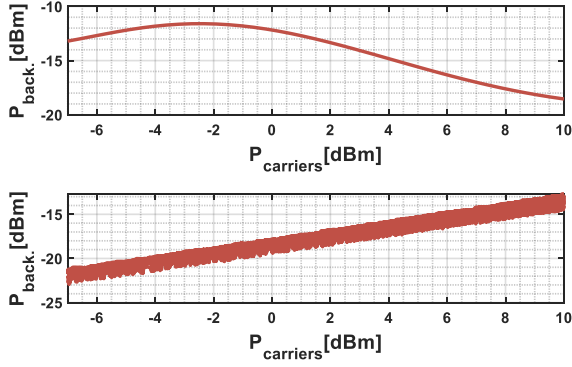


**Figure 7: Non-monotonic (top, passive RFID [37]) and monotonic backscatter radio (bottom, In-N-Out). The top figure is adapted from [37].**

To this end we design a low-power, monotonic backscatter radio. The hardware schematic is shown in Figure 6. Our backscatter radio contains two RF chains, one for energy harvesting (through antenna one) and another for backscatter (through antenna two). It allows the energy harvesting and backscatter to operate in parallel, without interfering each other. To achieve a consistent impedance, the RF power on the backscatter radio should be relatively stable. Hence we put a diode in-between these two modules, which allows the electric current to pass through in one direction (from the backscatter module to the energy harvesting module), while block it in the opposite direction. We measure the backscatter signal power as we gradually increase the carrier signal power. The result is shown in Figure 7. We observe that the backscatter signal power changes monotonically with the carrier signal, which confirms the effectiveness of the hardware design. The dynamic power consumption of this backscatter radio is  $42 \mu\text{W}$ , which takes up only around 12% of the energy harvested from our testbed ( $0.37 \text{ mW}$ ).

**4.1.3 Beamforming Power Change Inference.** The leader radio infers the power change of the beamforming signal by observing the power change of the received backscatter signal. A new challenge arises due to the extremely weak backscatter signal – after going through considerable channel fading, the backscatter signal is usually below the minimum detectable strength (MDS) of the commercial RF radios (e.g., around  $-75 \text{ dBm}$  for an USRP N210 software defined radio [6]). To verify this challenge, we put a backscatter radio into a 10 cm thick pork belly and conduct the following experiment. A transmitter node that is five meters away sends a continuous chirp pulse, with its power grows linearly from 0 to 20 dBm. A receiver node that is one meter away from the backscatter radio measures the received backscatter signal. Figure 8a plots the amplitude of the received backscatter signal. We observe noisy power measurements which fail to reflect the power change of the backscatter signal.

We define a new metric called  $P_{CCS(\omega)}$  and use it to infer the power change of the backscatter signal.  $P_{CCS(\omega)}$  is computed by correlating the received backscatter signal with the reference chirp in the frequency domain. We have proved that the peak value of  $P_{CCS(\omega)}$ , namely,  $P_{CCS(0)}$ , changes monotonically with the power

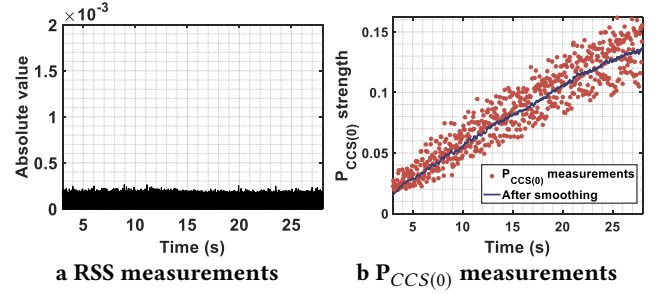


**Figure 8: (a) RSS and (b)  $P_{CCS(0)}$  measurements of the received backscatter signal as the carrier signal power grows linearly.**

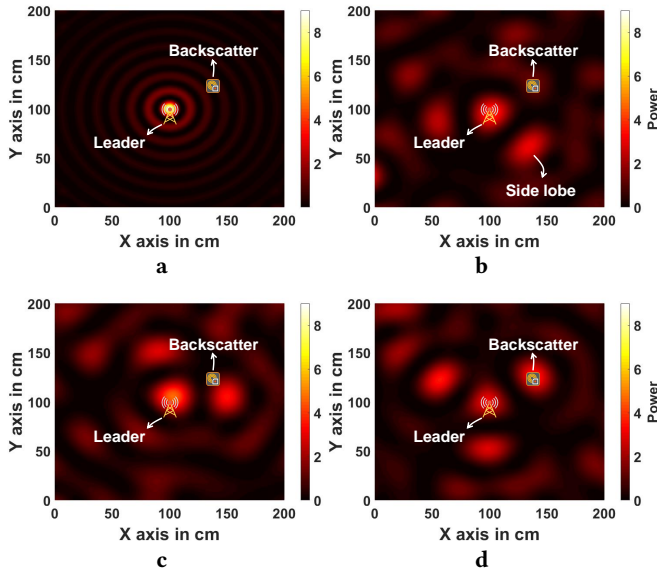
change of the backscatter signal, and demonstrated that  $P_{CCS(0)}$  has sufficient resolution to reflect the power change of the backscatter signal. Due to the page limitation, we put the mathematical proof in Appendix A.

Figure 8b shows  $P_{CCS(0)}$  samples extracted from the received signals. We observe an increasing trend of  $P_{CCS(0)}$  as we increase the power of carrier signal. However, due to signal noises and measurement errors,  $P_{CCS(0)}$  fluctuates drastically, which may confuse the leader radio and introduce extra beamforming iterations. To solve this problem, we adopt an adaptive Kalman filter [38] to smooth the  $P_{CCS(0)}$  samples. Figure 8b shows that the filtered samples can fairly reflect the power change of the backscatter signal.

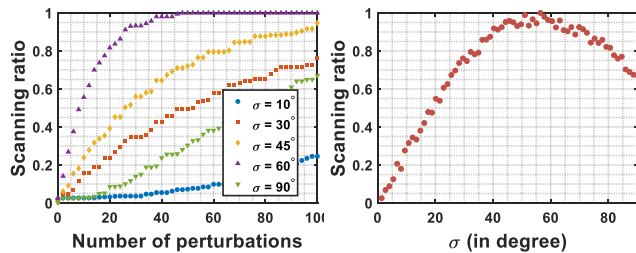
## 4.2 Cold Start

Previous sections focus on how to beamform towards the backscatter radio that is already awake. In this section, we describe how we bootstrap the backscatter radio during the cold start period. Cold start is a “chicken-n-egg” problem: without enough power ( $-20 \text{ dBm}$  at least [20]) the backscatter radio cannot wake up to provide feedback (by simply reflecting the signal). On the other hand, without the feedback, we cannot beamform to provide energy. Exhaustively searching all the beamforming space in hope of accidentally waking up the backscatter radio is obviously not a viable approach. Employing PushID [107] to wake up the backscatter radio, on the other hand, requires a much stronger carrier signal to compensate the excessive channel fading inside the human body, which may overheating human tissues and cause safety issues.

We propose a beamforming-based space searching algorithm to bootstrap the backscatter radio. Recall that the leader node can be a mobile phone or a wearable device worn by the user, it is thus reasonable to assume the leader node is close to the medical implant. In In-N-Out, we first align all beams towards the leader node and then search the limited space around the leader node. The space searching algorithm is based on the realization that different phase combining can lead to a significant different beamforming patterns. Specifically, let  $\phi_i$  be the current phase setting of the slave radio  $i$ . As we introduce a phase perturbation  $\delta_\phi$  to  $\phi_i$ , the carrier signals will coherently combine at other locations, resulting in side lobes. This new phase combination also spreads the main beamforming lobe over a larger area, as shown in Figure 9(b). Accordingly, by introducing different phase perturbation  $\delta_\phi$  ( $-\sigma < \delta_\phi < \sigma$ ) to each slave radio, we can produce different beamforming patterns and



**Figure 9: Beamforming energy patterns with different phase perturbations: (a) optimal phase alignment, (b)-(d) with different phase perturbations. With phase perturbations, we observe an enlarged main lobe and many side lobes. These side lobes can provide sufficient energy to wake up the backscatter radio.**



**a Scanning ratio CDF vs. number of perturbations** **b Scanning ratio values after 100 perturbations vs.  $\sigma$**   
**Figure 10: Phase perturbation range  $\sigma$  analysis.**

use them for space searching. When the backscatter radio gains enough energy as a result of this searching effort, it wakes up and starts to backscatter. Once the leader radio receives this backscatter signal, it goes back to serve its functions described in §4.1.1 and §4.1.3.

As the beamforming power spreads over the main lobe and side lobes, the question here is whether these lobes are strong enough to wake up the backscatter radio. To answer this question, we measure the power distribution of the beams shown in Figure 9(b)–(d) and find a 3.6 dB power drop with respect to the optimal beamforming power (Figure 9(a)). Note that to achieve a desirable charging efficiency, the optimal beamforming power of a multi-antenna system is much higher than the power required in the cold start period (–15 dBm). Hence, these newly emerging beams are strong enough to wake up the backscatter radio. Our micro-benchmark result (§6.1.2) also confirms the efficacy of this cold start method.

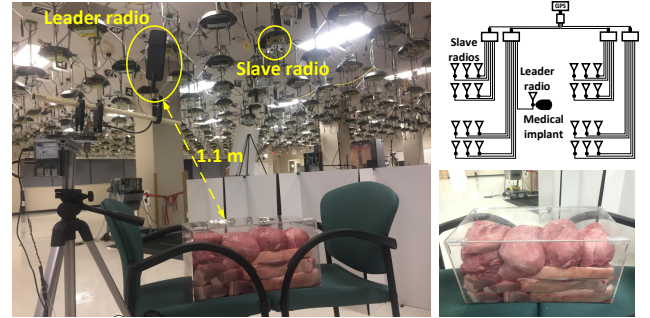


**Figure 11: Testbed setup. Our testbed consists of 17 USRP N210 and four USRP B210 nodes, all mounted on the ceiling of an office building.**

**Determining the phase perturbation range  $\sigma$ .** We define the scanned area as the space where the received energy is higher than 30% of the optimal beamforming power (equivalent to  $< 5$  dB loss). We then conduct simulations to investigate the impact of the phase perturbation range  $\sigma$  on the scanning ratio – the ratio of the scanned area to the entire searching space (a  $2 \times 2 \times 2$  m<sup>3</sup> Cube centered at the receiver). Figure 10(a) shows the scanning ratio as a function of phase adjustment in different  $\sigma$  settings. The scanning ratio grows rapidly as we increase  $\sigma$  from  $10^\circ$  to  $30^\circ$  and further to  $60^\circ$ . The growth of scanning ratio then slows down as  $\sigma$  increases further. To better understand this result, we further repeat the above experiment 100 times in different  $\sigma$  settings and show the result in Figure 10(b). We can see the scanning ratio peaks the maximal when  $45^\circ \leq \sigma \leq 65^\circ$ . Suggested by this simulation result, we set  $\sigma$  to  $55^\circ$ .

### 4.3 Balancing Convergence and Delay

In our iterative beamforming algorithm, the phase searching bound  $\Phi$  is critical to system performance ( $\Phi$  is introduced in §3). If  $\Phi$  is too large, the algorithm may rapidly converge to a non-optimal beamforming result. In contrast, a smaller  $\Phi$  will lead to better beamforming results, but with a longer delay. In In-N-Out, we use a larger phase bound at the beginning of the algorithm and then a smaller value as the algorithm iterates. We compute a suitable phase searching bound in each iteration based on a high order polynomial function  $\Phi = P(n)$ , where  $n$  is the iteration index. Due to page limitation, we detail this polynomial function and its derivation in Appendix B.

## 5 IMPLEMENTATION

We describe the system implementation in this section.

### 5.1 Testbed Setup

We deploy 17 USRP N210 and four USRP B210 software defined radios on the ceiling of an office building, as illustrated in Figure 11. Each USRP is equipped with a WBX RF daughter board [31] and works on FDD full duplex mode. We use a Mini-Circuits ZFL-1000VH RF amplifier [32] to boost the signal power and send out the amplified signal through a 4 dBi Taoglas TG.35.8113 antenna [11].

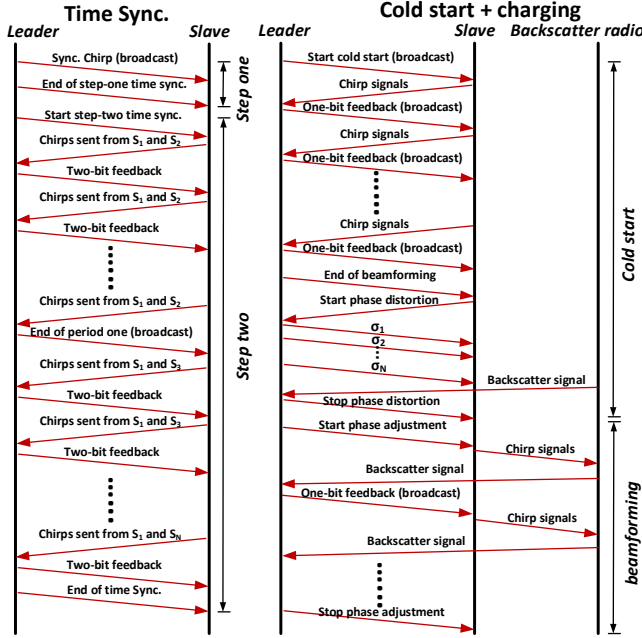


Figure 12: Message flow of In-N-Out.

As USRP only supports relative signal power measurement [7], we conduct a one-time power calibration using an Agilent E4405B spectrum analyzer [15] to acquire the absolute signal power.

**USRP Synchronization.** To mitigate the clock drift and carrier frequency offset (CFO), all USRPs are wired to an Octoclock-G GPS disciplined oscillator (GPSDO) [22] with 10MHz reference signal. This centralized time synchronization method provides an accurate timing reference. Wireless-based time synchronization methods such as [55, 90] can be further employed for an even larger system deployment.

## 5.2 Software Implementation

We implement all signal processing modules in C++ (version 4.8.4) with UHD driver V3.10.1 and GNU Radio Companion V3.7.6.1. Figure 12 shows the message flow of these signal processing modules. We next describe the module implementation on the leader radio and the slave radio.

**Leader radio** has three modules: chirp signal synchronization, backscatter radio cold start, and beamforming orchestration. We implement the following signal processing functions to support the above three modules: chirp preamble generation and transmission, RSS fluctuation detection, two-bit feedback signal generation and transmission, backscatter signal detection,  $P_{CCS(0)}$  calculation, smoothing, and comparison.

**Slave radios** participate in all the three modules mentioned above. We implement the following signal processing functions on each slave radio: chirp preamble detection, two-bit feedback signal detection and decoding, time calibration, beamforming signal detection, random number generator, phase adjustment, chirp carrier generation, and transmission.

## 5.3 RF Power Limit

Exposure to high levels of RF radiation can be harmful.

**Transmission power:** According to Federal Communications Commission (FCC) regulation, the transmission power of a single radio (with a 4 dBi antenna gain) should be below 32 dBm [16]. In our deployment, the maximum transmission power is 30 dBm and thus complies with the FCC regulation.

**Power density in space:** FCC and Food and Drug Administration (FDA) have different regulations for power density. Specifically, FCC requires the power density in ISM band to be below  $0.6 \text{ mW/cm}^2$  [1], whereas FDA requires the power density to be below  $10 \text{ mW/cm}^2$  [13]. In our testbed, 24 antennas are distributed on the ceiling of an  $18 \times 18 \text{ m}^2$  office building. The theoretically maximal power density at the receiver is  $0.08 \text{ mW/cm}^2$  based on [25], which satisfies both FCC and FDA requirements. In our experiments, we also measure the beamforming power at different locations across the room. The maximum measured power density is  $0.05 \text{ mW/cm}^2$ , well below the power limits specified by FCC and FDA.

## 6 EVALUATION

We present the evaluation results in this section. By default the chirp bandwidth and symbol time are set as 40 KHz and 4 ms (8192 samples), unless otherwise noted (when we investigate their impact on the system performance).

### 6.1 Micro-benchmark

We start with performing micro-benchmarks to evaluate the effectiveness of each function module in In-N-Out.

**6.1.1 Chirp Synchronization.** Experiments in this section aim to i) evaluate the overall performance of the two-step chirp synchronization algorithm, and ii) understand the relationship between synchronization delay and number of slave radios.

**i). The accuracy of chirp synchronization algorithm.** We synchronize chirp signals from all 24 slave radios using the two-step chirp synchronization algorithm. We repeat this experiment 100 times and plot the CDF of the residual time offsets before and after applying our algorithm in Figure 13. Without chirp synchronization, the median and maximum time offsets are 3630 and 8182 samples, respectively. These two values drop to around 86 and 168 samples after the first-step chirp synchronization, and 0.4 and 0.9 sample after the second-step chirp synchronization. The trend clearly demonstrates that our chirp synchronization algorithm can effectively calibrate out the initial time offset among radios.

**ii). Synchronization delay vs. slave count.** We then evaluate the chirp synchronization delay (termed as delay) under a different number of slave radios. We repeat this experiment 100 times in each setting and plot the results in Figure 14. We observe the delay increases with the number of slave radios. Specifically, the delay is below 1.4 s when we have six slave radios, 2.9 s for 12 slaves, 5.3 s for 18 slaves, and 6.4 s for 24 slaves. Please note that our chirp synchronization needs to run only once, and the one-time delay of 6.4 s would not have a noticeable effect on the user experience.



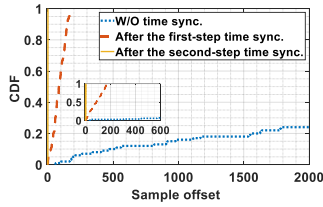


**Figure 13: CDF of residual time offset without and with chirp synchronization.**

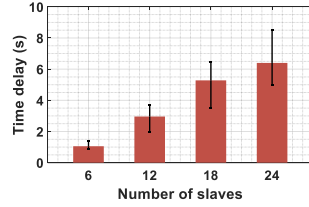


**Figure 14: Chirp synchronization delay vs. number of slave radios.**

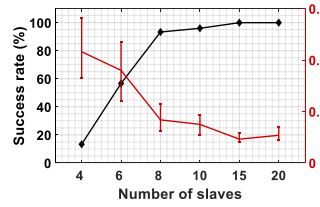


**Figure 15: Cold start success rate (left) and delay (right) vs. number of slave radios.**

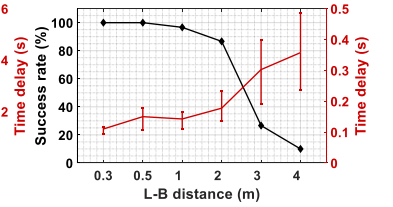


**Figure 16: Cold start success rate (left) and delay (right) vs. L-B distance.**

**6.1.2 Cold Start.** Experiments in this section aim to evaluate the cold start success rate and delay when we vary i) number of slave radios and ii) distance between the leader and the backscatter (termed as L-B distance).

**i). Success rate and delay vs. slave count.** In these experiments, we insert a backscatter radio into a 10 cm-thick pork belly and cold start it using a different number of slave radios. The leader radio is half a meter away from this pork belly. We perform this experiment 100 times in each setting and plot the success rate and delay in Figure 15. We observe the success rate is low when we use only four slave radios. This is as expected since beamforming power of four slave radios is too low. The success rate soon jumps to 90% as we double the number of slave radios. It then approaches to 100% when the slave count is larger than 15. These results demonstrate the effectiveness of our cold start algorithm. On the other hand, we see the delay of cold start decreases as we increase the number of slave participants. The longest delay, however, is only 0.56 s. These results clearly demonstrate the effectiveness of our cold start algorithm.

**ii). Success rate and delay vs. L-B distance.** We then test success rate and delay of our cold start algorithm in different L-B distance settings. In these experiments, we insert a backscatter radio into a 10 cm-thick pork belly and cold start it using 10 slave radios. Results are shown in Figure 16. The success rate is around 100% when the leader radio is close to the backscatter radio, e.g., 0.3 m and 0.5 m away. It then decreases slightly to 96.7% and further to 86.6% as we increase the L-B distance to 1 m and 2 m, respectively. We observe a significant performance degradation (from 96.7% to 26.3%) when the leader is 3 m away from the backscatter radio. This is because the searching space is too large, hence the power of side lobes is not strong enough to wake up the backscatter radio. As for cold start delay, we observe that it grows smoothly as we increase the L-B distance from 0.3 m to 2 m. It then jumps to around 0.3 s and further to 0.35 s as we place the leader radio 3 m and 4 m away from the backscatter radio, respectively. By default, the leader radio is placed less than 1 m away from the human body. This is very practical because in real life, the leader radio can simply be the smartphone carried by the target or the smartwatch on the target's wrist. These devices are usually less than 1 m away from the implant inside the body.

**6.1.3 Beamforming.** Experiments in this section aim to evaluate the delay and power gain of our beamforming algorithm in various parameter settings, e.g., different number of slave radios and different chirp bandwidths. To measure the power gain gap between

our beamforming algorithm and the optimal one, we define a new metric, namely *power percentage*, as the square of the ratio between the averaged beamforming amplitude (achieved by In-N-Out) and the optimal beamforming amplitude. In reality, however, the optimal beamforming amplitude cannot be measured directly. We thus start each slave radio at a time and record the received signal amplitude at the backscatter radio. The summation of these signal amplitudes serves as an alternative to the optimal beamforming amplitude. We also define the *beamforming delay* as the execution time of our beamforming algorithm until the beamforming power at the backscatter radio converges.

**i). Close to optimal beamforming amplitude.** We measure the beamforming amplitude gap between our algorithm and the optimal one. In this demonstrating experiment, we run our beamforming algorithm on three slave radios. The backscatter radio is inserted into a 10 cm thick pork belly placed 2 m away from each slave radio. For a better illustration, we sequentially start these three slaves and measure their signal amplitude at the backscatter radio. Figure 17 shows the result. We can see the beamforming amplitude grows rapidly and converges to a large value. The convergence signal amplitude (dashed line) stays closely to the optimal beamforming amplitude (dotted line), with the average amplitude percentage of 96.5%. This result clearly demonstrates the high efficiency of the proposed beamforming algorithm.

**ii). Convergence delay vs. slave count.** Short convergence delay is crucial to our system, especially in mobile scenarios. We next examine the impact of slave count on the resulting beamforming delay. The experiment setup follows the previous experiment. We run the beamforming algorithm 100 times in each setting and plot the delay in Figure 18. As we can see, the beamforming delay grows slowly as we increase the number of slave radios. Specifically, the average delay is 0.15 s, 0.21 s, 0.25 s and 0.33 s with 6, 12, 18 and 24 slave radios, respectively. Further, we observe that though the beamforming delay fluctuates from experiment to experiment, the maximum delay is less than 0.41 s. Hence, we believe that our iterative beamforming algorithm is fast enough for most of the in-body charging scenarios.

**iii). Power percentage vs. chirp bandwidth.** We then examine the impact of chirp bandwidth on the beamforming power percentage. Similar to previous experiments, the backscatter radio is inserted into a 15 cm thick pork belly placed 2 m away from 20 slave radios that are randomly picked from our testbed. We run the experiment 100 times in each setting and plot the achieved power percentage values in Figure 19. As shown, the power percentage

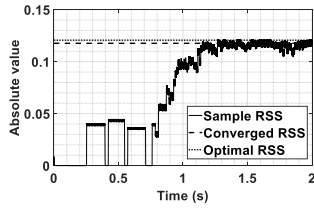


Figure 17: RSS during a beamforming episode.



Figure 18: Beamforming delay vs. number of slave radios.

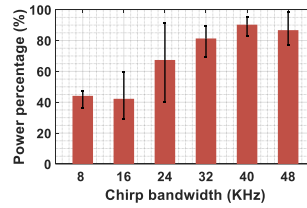


Figure 19: Power percentage vs. chirp bandwidth.

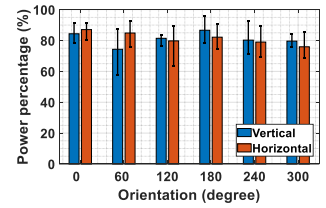


Figure 20: Power percentage vs. backscatter orientation.

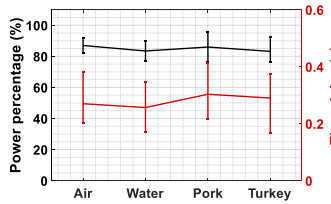


Figure 21: Power percentage across different media.

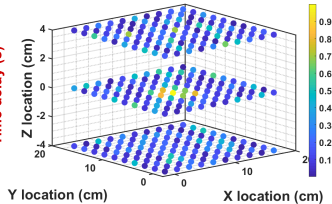


Figure 22: In-tissue 3D power distribution.

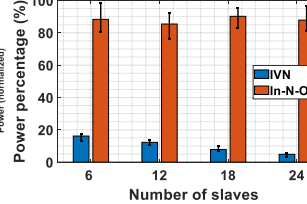


Figure 23: Power percentage vs. slave count.

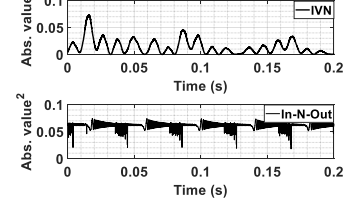


Figure 24: Beamforming power samples.

grows as we first increase the chirp bandwidth – a higher chirp bandwidth improves the accuracy of the power inference algorithm. An accurate power inference result further improves the beamforming efficiency. Meanwhile, we observe that the power percentage increase rate decreases with the chirp bandwidth, indicating that the marginal utility of the frequency-domain processing gain decreases. Considering both trends, we set 40 KHz as the default chirp bandwidth setting.

**iv). Power percentage vs. backscatter radio orientation.** We further examine how the backscatter radio’s orientation affects the beamforming efficiency, which also indicates our system’s robustness against the radio placement. In these experiments, we rotate the backscatter radio (inside a 15 cm thick pork belly) horizontally and vertically from  $0^\circ$  to  $300^\circ$  and measure the power percentage at the backscatter radio. We repeat the experiment 100 times in each rotation angle and plot the results in Figure 20. We observe that In-N-Out achieves a consistently high power percentage (an average of 83.5%, minimum of 74.3% and maximum of 87.1%) in all rotation angle settings. This is because the antennas in our system are placed in a distributed fashion and thus are insensitive to the backscatter radio orientation.

**v). Sufficient power for commercial medical implants.** To examine whether the beamforming power achieved by In-N-Out is sufficient to charge commercial medical implant, we conduct a survey on the power consumption of several representative medical implants [34, 54], including pacemaker, cardiac defibrillator, neuro-stimulator, and controlled internal drug release (CIDR). For comparison, we also calculate the average beamforming power (in  $\mu\text{W}$ -scale) achieved by In-N-Out. Table 2 summarize the result. We measured  $107 \mu\text{W}$ – $617 \mu\text{W}$  (average  $372 \mu\text{W}$ ) beamforming power across the  $18 \times 18 \text{ m}^2$  testbed area. The available power is higher than the power consumption of pacemakers and cardiac defibrillators, and only slightly lower than some neuro-stimulator and CIDR devices. We envision by shortening the signal propagation

Device	Pacemaker	Cardiac defibrillator	neuro-stimulator	CIDR	In-N-Out
Power ( $\mu\text{W}$ )	10–100	25–250	40–500	100–800	372

Table 2: Power requirements of several commercial medical implants. In-N-Out can achieve average  $372 \mu\text{W}$  by using 24 slave radios, which is sufficient to power up most of commercial pacemakers and cardiac defibrillators, as well as many neuro-stimulators and CIDRs.

path, such as deploying the system in smaller areas such as bedrooms or offices, In-N-Out would achieve a substantially higher beamforming power.

## 6.2 Field Study

We next conduct field studies to evaluate the performance of In-N-Out in different mediums. Although there are a surge of inbody wireless charging competitors, we choose the state-of-the-art work IVN [77] for comparison as IVN shares the most similar hardware setup with In-N-Out. We carefully implement IVN and compare the performance of these two approaches in both stationary and mobile scenarios.

**i). Impact of Medium.** We first examine whether our system can be used in other media. In these experiments, we place the backscatter radio in four different media with significantly different channel characteristics, *i.e.*, air, water, pork and turkey. We measure the resulting power percentage and delay (excluding chirp synchronization) of our system in each setting. 24 slave radios are involved in these experiments. As shown in Figure 21, In-N-Out achieves the highest average power percentage in the air (86%), followed by 85% in the water, 83% in the pork belly, and finally 83% in the turkey. While the beamforming delays in these four media are slightly different, they are all below 0.41 s and would not cause noticeable delays in most of the cases. These experiment results demonstrate that In-N-Out can be used to charge objects in various media.

**ii). In-tissue Power Distribution** We then examine In-N-Out’s power distribution in deep tissues. The backscatter radio is placed



Figure 25: Experimental setup for mobile cases.

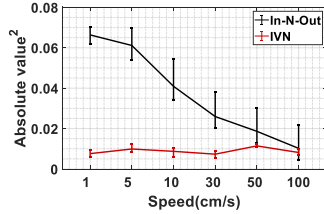


Figure 26: Average beamforming power vs speed.

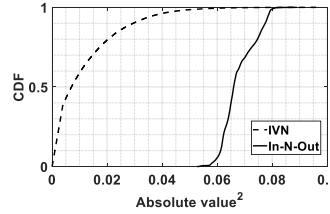


Figure 27: CDF of the beamforming power. ( $v = 5$  cm/s)

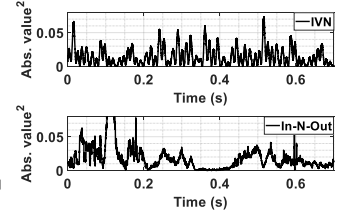


Figure 28: Beamforming power samples. ( $v = 1$  m/s)

inside a 10 cm-thick pork belly. Figure 22 shows the power distribution measured across three slices (with 10 cm depth) of the pork belly. The backscatter radio is placed at (8, 8, 0). We observe a clear hot spot around the backscatter radio (with a radius around 2 cm) in the 3D space where the beamforming power is the highest. The power at other locations, however, stays at a relatively low level. The average power at the hot spot is  $10.3\times$  higher than the average power measured at the other locations. This result clearly demonstrates that In-N-Out can successfully concentrate the beamforming energy to a tiny energy spot in a non-uniform medium like pork belly.

**iii). Comparison with IVN in stationary cases.** We first compare the power gain of In-N-Out and IVN in stationary cases. In these experiments, we insert a backscatter radio into a 10 cm thick pork belly and place them on a stationary table. We then vary the number of slave radios from 6 to 24 and measure the power percentage achieved by both In-N-Out and IVN. The experiment setup stays the same as the setup in the previous experiment. We repeat this experiment 100 times in each setting and plot the results in Figure 23. As shown, In-N-Out achieves a consistently higher power percentage than IVN. Specifically, when we have 6 slave radios, the average power percentage achieved by In-N-Out is 87.32%,  $5.4\times$  higher than that achieved by IVN (16.2%). When we triple the number of slave radios (18), In-N-Out achieves  $12.8\times$  higher power percentage than IVN. This gap further increases ( $18.1\times$ ) as we use 24 slave radios.

To better understand the performance gap, we profile the instantaneous beamforming power of these two approaches and show the result in Figure 24. Both IVN and In-N-Out can achieve high beamforming power, but IVN only achieves high power levels at some time points. Its power level in most of the time, including the charging period, stays rather low, leading to a low average power level. In contrast, the beamforming power achieved by In-N-Out is rather consistent, hence a much higher average power level.

**iv). Comparison with IVN in Mobile Cases.** We further conduct the performance comparison in mobile cases where the charging target moves around during the charging process. In these experiments, we put a backscatter radio inside a 21 lb turkey. The turkey is then fixed on a Pioneer-p3dx robot [4] running ROS (Robot Operating System) [89]. Figure 25 shows the mobile experiment setup. We use 10 slave radios and measure the received power level at the backscatter radio while the robot moves around. The experiment is repeated 100 times in each speed setting. Figure 26 shows the average power achieved by In-N-Out and IVN. When the robot moves at a relatively slow speed (e.g., 1 cm/s and 5 cm/s), In-N-Out

outperforms IVN by  $7.4\times$  and  $5.3\times$ , respectively. To understand this difference, we plot the CDF of the beamforming power of these two systems when the robot moves at 5 cm/s. The result is shown in Figure 27. For In-N-Out, we find its power level stays rather consistent, with the lowest and highest power level of 0.053 and 0.089. In contrast, the power level variation of IVN is much larger, with its 90% percentile value below 0.029. This result demonstrates that In-N-Out is agile enough to handle the target's slow movement, e.g., moving with the blood flowing.

As we increase the speed, the performance gap between these two systems decreases. Specifically, when the robot moves at 1 m/s, the two approaches deliver similar power levels. To understand this trend, we randomly select a 0.8 s time window and measure the instantaneous beamforming power levels, as shown in Figure 28. The results show that at such a high speed, the power levels by both approaches vary drastically. However, we expect that lower movement speeds such as 1 cm/s and 5 cm/s are much more commonplace than speeds as high as 1 m/s in medical implant charging scenarios. We believe In-N-Out can handle such common cases successfully.

## 7 RELATED WORK

Our system is related to wireless charging and backscatter, while quantitatively differ from either one.

### 7.1 Wireless Charging in Bioelectronics

Wireless charging in bio-electronics can be broadly divided into three categories: near-field inductive coupling, far-field electromagnetic radiation, and others.

**Near-field inductive coupling** exploits magnetic field induction effect to deliver energy between two coils [73]. Research works in this domain focus on inductive power link optimization [64, 73, 92, 108], source-load decoupling [91], and multi-coil linkage design [63, 68]. While near-field method achieves satisfying power delivery efficiency, it requires the user to wear bulky coils and align them with the implanted coil [10]. As a result, the users need to sit still for hours to have their implants fully charged. Moreover, the charging efficiency of near-field methods drops significantly with the reduction of coil size, which limits their working range to less than a centimeter [35, 56]. Hence the focus in this field has shifted towards overcoming the coil misalignment problem and improving the system robustness.

**Far-field wireless charging** transfers power to the target through electromagnetic radiation [41, 45, 75], microwave radiation [65], or laser [61, 62]. Compared to the near-field method, the far-field

method supports wireless charging over a longer distance at the cost of lower wireless charging efficiency. Research in this field focuses on RF diode and DC impedance optimization [45], antenna optimization [75], and effective system implementation [41]. IVN [77] introduces an opportunistic frequency-encoding method in hope of combining signals constructively at the medical implant. However, IVN's beamforming power, for most of the time, is far below the maximum value it can potentially achieve. In contrast, In-N-Out aligns the phase of signals at the medical implant rapidly and keeps this coherent phase combining over the entire wireless charging period. Hence it can continuously charge the medical implant with consistently near-optimal beamforming power. The different design principle of In-N-Out and IVN leads to a significant gap in power delivery efficiency: In-N-Out achieves  $5.4 - 18.1\times$  and  $5.3 - 7.4\times$  power gain over IVN in stationary and mobile case, respectively.

In-N-Out also builds upon past works that leverage one-bit phase alignment algorithm [47, 82] for wireless charging. Energy-ball [47] adopts this algorithm to charge IoT devices where CSI is unavailable. WiFED [82] employs this algorithm to realize near optimal power transferring and communication over Wi-Fi links. However, both of these pioneer works assume the receiver has enough battery to assess the beamforming power and produce feedback signals, which is not true for the ultra-low power, energy-scarce medical implants. Besides, the excessive link budget renders the feedback signal far below the noise floor, and thus fail the feedback signal detection and decoding on the transmitter side. Accordingly, we cannot directly borrow these techniques for inbody wireless charging.

As another alternative, mid-field resonant power transfer that combines both near-field and far-field methods is proposed [59, 71, 71, 88]. While this method can work over longer distances in the free space, the working range in the human body is still constrained by the coil spacing. Although the focus of this review is on RF-based methods, there are also related works on leveraging ultrasound for power transfer [50, 51, 80, 95, 96, 101]. In [51, 80, 101], the authors demonstrate the feasibility and advantages of ultrasonic power charging for implanted devices in animal tissues and tissue mimicking materials. In [50, 95, 96], the authors proposed end-to-end ultrasonic charging and communication systems, whereas they focus on protocol design, hardware form-factor minimization and system rechargeability. Although ultrasound-based methods achieve higher power transfer efficiency, they are still intrusive due to the requirement of placing the transmitter coil close to the receiver (e.g., attach to the human skin).

## 7.2 Backscatter Communication

Backscatter systems encode information on top of the remote carrier signal for ultra-low-power communication. Recent studies on backscatter communication aim to improve the backscatter range [79, 87, 102], enhance the ubiquity [58, 66, 76, 103, 109], and enable new applications such as fine-grained localization [78, 98, 105], material identification [53, 106], and vehicle counting and localization [33]. In-N-Out takes advantage of the backscatter design to reduce the energy consumption of the medical implant.

There are also several works studying wireless charging on backscatter node without explicit channel measurement [37, 42]. However, these works still require CSI measurement at transmitters, which is very challenging due to the severe signal attenuation in

deep tissues. In-N-Out addresses this challenge by precoding the carrier signal using chirp modulation and leveraging its unique processing gain in the frequency domain to improve the SNR of backscatter signals. Additionally, In-N-Out introduces a new metric  $P_{CCS(0)}$  to replace the unreliable power measurement, and uses this metric to guide the execution of beamforming algorithm.

## 8 DISCUSSION

In-N-Out leaves room for further investigations, as discussed below:

**Reducing deployment cost** As a proof-of-concept, we implement In-N-Out on software-defined radios (*i.e.* USRP) for fast-prototyping. In the future we plan to customize the RF radio design to reduce the overall system cost. Given the light-weight computation tasks and narrow band communication nature of our system, one can customize the RF radio with a MSP430 [21] MCU (\$2.09), a MAX2235 [19] power amplifier (\$2.16), a TI SN74LS624N [26] oscillator (\$3.94), two cc1100 [12] radio transceivers (\$3.65), and two W5017 [29] antennas (\$7.25), which leads to a total cost around \$25.

**Scaling to multiple targets.** While the system design is illustrated in the single target settings, In-N-Out can be easily extended to multi-user scenario by introducing a MAC layer protocol such as time duplex multiple access (TDMA) or Frequency duplex multiple access (FDMA). We leave this for our future work.

## 9 CONCLUDING REMARKS

In this paper, we present the design, implementation, and evaluation of In-N-Out: a multi-antenna system that can continuously charge the medical implant at the near optimal beamforming power, even when the implant moves around inside the human body. To achieve this, In-N-Out proposes a set of novel signal processing algorithms and a low-power, monotonic backscatter radio design. We prototype In-N-Out on software defined radios and PCB boards. The head-to-head comparison on a multi-antenna testbed demonstrates that In-N-Out achieves  $5.4\times-18.1\times$  and  $5.3\times-7.4\times$  average power gain over the state-of-the-art solution in stationary and low-speed mobile scenarios, respectively. In-N-Out is the first step towards flexible wireless charging for medical implants. Moving forward, we will endeavor to address the following technical challenges: achieving optimal deployment of the antenna array, mitigating the impact of strong multi-path effects, charging multiple implants simultaneously, etc. We also plan to pursue subsequent clinical experiments for further validations.

## ACKNOWLEDGEMENTS

We thank the reviewers and our shepherd for their insightful comments. We also thank Dr. Lin Zhong for providing us useful feedback on the early version of this work. This work is supported by the Key Research Program of Frontier Sciences, CAS, Grant No.ZDBS-LY-JSC001 and partially supported by 2030 National Key AI Program of China Grant No. 2018AAA0100500. Corresponding author: yanyongz@ustc.edu.cn

## REFERENCES

- [1] 1997. OET Bulletin No. 65 (August 1997). Webpage.
- [2] 2005. Nuclear power battery lasts 12 years. Webpage.
- [3] 2009. Cochlear Implants. Webpage.
- [4] 2011. Pioneer 3-DX robot. Webpage.
- [5] 2012. Pacemaker battery replacement causes cardiac arrest. Webpage.
- [6] 2012. USRP N210 minimum detectable signal strength. Webpage.
- [7] 2015. Compare your daughterboard's data from. Webpage.
- [8] 2017. Expected lifetime analysis for medical devices. Webpage.
- [9] 2017. LoRaWAN Specification v1.3. Webpage.
- [10] 2018. Wirelessly charging medical devices breakthrough brings new solution. Webpage.
- [11] 2019. Apex II TG.35 antenna . Webpage.
- [12] 2019. cc1100 Datasheet. Webpage.
- [13] 2019. CFR - Code of Federal Regulations Title 21. Webpage.
- [14] 2019. Cross-correlation . Webpage.
- [15] 2019. E4405B ESA-E spectrum analyzer. Webpage.
- [16] 2019. FCC Rules for Unlicensed Wireless Equipment operating in the ISM bands. Webpage.
- [17] 2019. Gastroscopy. Webpage.
- [18] 2019. Implants and Prosthetics. Webpage.
- [19] 2019. MAX2235 Datasheet. Webpage.
- [20] 2019. Monza r6 datasheet. Webpage.
- [21] 2019. MSP430 Datasheet. Webpage.
- [22] 2019. OctoClock-G CDA-2990. Webpage.
- [23] 2019. Pacemaker. Webpage.
- [24] 2019. Prosthesis. Webpage.
- [25] 2019. RF power density calculator. Webpage.
- [26] 2019. SN74LS624N Datasheet. Webpage.
- [27] 2019. The real-life applications of IoT and why battery life is critical. Webpage.
- [28] 2019. Transvaginal mesh to fix pelvic organ prolapse. Webpage.
- [29] 2019. W5017 Datasheet. Webpage.
- [30] 2019. Wardencliff Tower. Webpage.
- [31] 2019. WBX 50-2200 MHz Rx/Tx (40 MHz). Webpage.
- [32] 2019. ZFL-1000VH+ 10-1000 MHz high dynamic range RF amplifier. Webpage.
- [33] Omid Abari, Deepak Vasisht, Dina Katabi, and Anantha Chandrakasan. 2015. Caraoke: An e-toll transponder network for smart cities. In *ACM SIGCOMM*.
- [34] Achraf Amar, Ammar Kouki, and Hung Cao. 2015. Power approaches for implantable medical devices. *sensors* (2015).
- [35] Amin Arbabian, Ting Chia Chang, Max L Wang, Jayant Charthad, Spyridon Baltasvias, Mojtaba Fallahpour, and Marcus J Weber. 2016. Sound technologies, sound bodies: Medical implants with ultrasonic links. *IEEE Microwave Magazine* (2016).
- [36] Michel Armand and J-M Tarascon. 2008. Building better batteries. *nature* (2008).
- [37] Daniel Arnitz and Matthew S Reynolds. 2013. Wireless power transfer optimization for nonlinear passive backscatter devices. In *IEEE RFID*.
- [38] Robert Grover Brown, Patrick YC Hwang, et al. 1992. *Introduction to random signals and applied Kalman filtering*. Wiley New York.
- [39] William C Brown. 1965. *Experimental airborne microwave supported platform*. Technical Report. DTIC Document.
- [40] Hyouk-Kyu Cha, Woo-Tae Park, and Minkyu Je. 2012. A CMOS rectifier with a cross-coupled latched comparator for wireless power transfer in biomedical applications. *IEEE Transactions on Circuits and Systems II: Express Briefs* (2012).
- [41] Eric Y Chow, Arthur L Chlebowski, Sudipto Chakraborty, William J Chappell, and Pedro P Irazoqui. 2010. Fully wireless implantable cardiovascular pressure monitor integrated with a medical stent. *IEEE Transactions on Biomedical Engineering* (2010).
- [42] Eckhard Denicke, Henning Hartmann, Nikolai Peitzmeier, and Bernd Geck. 2018. Backscatter Beamforming: A Transponder for Novel MIMO RFID Transmission Schemes. *IEEE Journal of Radio Frequency Identification* (2018).
- [43] J Maxwell Donelan, Qinghua Li, Veronica Naing, JA Hoffer, DJ Weber, and Arthur D Kuo. 2008. Biomechanical energy harvesting: generating electricity during walking with minimal user effort. *Science* (2008).
- [44] Ilka Dove. 2014. *Analysis of radio propagation inside the human body for in-body localization purposes*. Master's thesis. University of Twente.
- [45] Erez Falkenstein, Michael Roberg, and Zoya Popovic. 2012. Low-power wireless power delivery. *IEEE Transactions on microwave theory and techniques* (2012).
- [46] Xiaoran Fan. 2019. Facilitating the Deployment of Next Billion IoT Devices with Distributed Antenna Systems. In *The ACM MobiSys 2019 on Rising Stars Forum*.
- [47] Xiaoran Fan, Han Ding, Sugang Li, Michael Sanzari, Yanyong Zhang, Wade Trappe, Zhu Han, and Richard E Howard. 2018. Energy-Ball: Wireless Power Transfer for Batteryless Internet of Things through Distributed Beamforming. *Proceedings of the ACM on Interactive, Mobile, Wearable and Ubiquitous Technologies* (2018).
- [48] Xiaoran Fan, Zhenzhou Qi, Zhenhua Jia, and Yanyong Zhang. 2018. Enabling concurrent iot transmissions in distributed e-ran. In *ACM SenSys*.
- [49] Xiaoran Fan, Zhijie Zhang, Wade Trappe, Yanyong Zhang, Richard E Howard, and Zhu Han. 2018. Secret-focus: A practical physical layer secret communication system by perturbing focused phases in distributed beamforming. In *IEEE INFOCOM*.
- [50] Raffaele Guida, Neil Dave, Francesco Restuccia, Emre Can Demirors, and Tommaso Melodia. 2019. U-Verse: a miniaturized platform for end-to-end closed-loop implantable internet of medical things systems. In *ACM SenSys*.
- [51] Raffaele Guida, G Enrico Santagati, and Tommaso Melodia. 2016. A 700 kHz ultrasonic link for wireless powering of implantable medical devices. In *IEEE SENSORS*.
- [52] Enes Elvin Gul and Mehmet Kayrak. 2011. Common pacemaker problems: lead and pocket complications. In *Modern Pacemakers-Present and Future*. InTech.
- [53] Unsoo Ha, Yunfei Ma, Zexuan Zhong, Tzu-Ming Hsu, and Fadel Adib. 2018. Learning Food Quality and Safety from Wireless Stickers. In *ACM HotNets*.
- [54] Daniel Halperin, Thomas S Heydt-Benjamin, Benjamin Ransford, Shane S Clark, Benessa Defend, Will Morgan, Kevin Fu, Tadayoshi Kohno, and William H Maisel. 2008. Pacemakers and implantable cardiac defibrillators: Software radio attacks and zero-power defenses. In *IEEE Symposium on Security and Privacy*.
- [55] Ezzeldin Hamed, Hariharan Rahul, and Bahar Partov. 2018. Chorus: truly distributed distributed-MIMO. In *ACM SIGCOMM*.
- [56] Mohammad A Hannan, Saad Mutashar, Salina A Samad, and Aini Hussain. 2014. Energy harvesting for the implantable biomedical devices: issues and challenges. *Biomedical engineering online* (2014).
- [57] Marcos Hervás, Rosa Alsina-Pagès, Ferran Orga, David Altadill, Joan Pijoan, and David Badia. 2015. Narrowband and wideband channel sounding of an Antarctica to Spain ionospheric radio link. *Remote Sensing* (2015).
- [58] Mehrdad Hesar, Ali Najafi, and Shyamnath Gollakota. 2019. NetScatter: Enabling Large-Scale Backscatter Networks.. In *USENIX NSDI*.
- [59] John S Ho, Alexander J Yeh, Evgenios Neofytou, Sanghoek Kim, Yuji Tanabe, Bhagat Patlolla, Ramin E Beygui, and Ada SY Poon. 2014. Wireless power transfer to deep-tissue microimplants. *Proceedings of the National Academy of Sciences* (2014).
- [60] Pan Hu, Pengyu Zhang, Mohammad Rostami, and Deepak Ganesan. 2016. Braidio: An integrated active-passive radio for mobile devices with asymmetric energy budgets. In *ACM SIGCOMM*.
- [61] Vikram Iyer, Elyas Bayati, Rajalakshmi Nandakumar, Arka Majumdar, and Shyamnath Gollakota. 2018. Charging a Smartphone Across a Room Using Lasers. *Proceedings of the ACM on Interactive, Mobile, Wearable and Ubiquitous Technologies* (2018).
- [62] Vikram Iyer, Rajalakshmi Nandakumar, Anran Wang, Sawyer B Fuller, and Shyamnath Gollakota. 2019. Living IoT: A Flying Wireless Platform on Live Insects. In *ACM MobiCom*.
- [63] Jouya Jadian and Dina Katabi. 2014. Magnetic MIMO: How to charge your phone in your pocket. In *ACM MobiCom*.
- [64] Uei-Ming Jow and Maysam Ghovanloo. 2007. Design and optimization of printed spiral coils for efficient transcutaneous inductive power transmission. *IEEE Transactions on biomedical circuits and systems* (2007).
- [65] Aristeidis Karalis, John D Joannopoulos, and Marin Soljačić. 2008. Efficient wireless non-radiative mid-range energy transfer. *Annals of physics* (2008).
- [66] Bryce Kellogg, Vamsi Talla, Shyamnath Gollakota, and Joshua R Smith. 2016. Passive Wi-Fi: Bringing Low Power to Wi-Fi Transmissions.. In *USENIX NSDI*.
- [67] Wahid Khan, Eameema Muntimadugu, Michael Jaffe, and Abraham J Domb. 2014. Implantable medical devices. In *Focal controlled drug delivery*. Springer.
- [68] Mehdi Kiani, Uei-Ming Jow, and Maysam Ghovanloo. 2011. Design and optimization of a 3-coil inductive link for efficient wireless power transmission. *IEEE transactions on biomedical circuits and systems* (2011).
- [69] Chee Wee Kim and Terence Shie Ping See. 2011. RF transmission power loss variation with abdominal tissues thicknesses for ingestible source. In *IEEE Healthcom*.
- [70] Jaehoon Kim and Yahya Rahmat-Samii. 2004. Implanted antennas inside a human body: Simulations, designs, and characterizations. *IEEE Transactions on microwave theory and techniques* (2004).
- [71] Sanghoek Kim, John S Ho, Lisa Y Chen, and Ada SY Poon. 2012. Wireless power transfer to a cardiac implant. *Applied Physics Letters* (2012).
- [72] Asimina Kiourti and Konstantina S Nikita. 2012. A review of implantable patch antennas for biomedical telemetry: Challenges and solutions [wireless corner]. *IEEE Antennas and Propagation Magazine* (2012).
- [73] Andre Kurs, Aristeidis Karalis, Robert Moffatt, John D Joannopoulos, Peter Fisher, and Marin Soljačić. 2007. Wireless power transfer via strongly coupled

- magnetic resonances. *science* (2007).
- [74] Bert Lenaerts and Robert Puers. 2007. An inductive power link for a wireless endoscope. *Biosensors and Bioelectronics* (2007).
- [75] Changrong Liu, Yong-Xin Guo, Hucheng Sun, and Shaoqiu Xiao. 2014. Design and safety considerations of an implantable rectenna for far-field wireless power transfer. *IEEE Transactions on antennas and Propagation* (2014).
- [76] Vincent Liu, Aaron Parks, Vamsi Talla, Shyamnath Gollakota, David Wetherall, and Joshua R Smith. 2013. Ambient backscatter: wireless communication out of thin air. In *ACM SIGCOMM* (2013).
- [77] Yunfei Ma, Zhihong Luo, Christoph Steiger, Giovanni Traverso, and Fadel Adib. 2018. Enabling Deep-Tissue Networking for Miniature Medical Devices. In *ACM SIGCOMM*.
- [78] Yunfei Ma, Nicholas Seby, and Fadel Adib. 2017. Minding the billions: Ultra-wideband localization for deployed rfid tags. In *ACM MobiCom*.
- [79] Yunfei Ma, Nicholas Selby, and Fadel Adib. 2017. Drone relays for battery-free networks. In *ACM SIGCOMM*.
- [80] Teimour Maleki, Ning Cao, Seung Hyun Song, Chinghai Kao, Song-Chu Ko, and Babak Ziaie. 2011. An ultrasonically powered implantable micro-oxygen generator (IMOG). *IEEE transactions on Biomedical Engineering* (2011).
- [81] Venkateswara Sarma Mallela, V Ilankumaran, and N Srinivasa Rao. 2004. Trends in cardiac pacemaker batteries. *Indian pacing and electrophysiology journal* (2004).
- [82] Subhramoy Mohanti, Elif Bozkaya, M Yousof Naderi, Berk Canberk, and Kaushik Chowdhury. 2018. WiFED: WiFi Friendly Energy Delivery with Distributed Beamforming. In *IEEE INFOCOM*.
- [83] Raghuraman Mudumbai. 2007. *Energy efficient wireless communication using distributed beamforming*. University of California, Santa Barbara.
- [84] Raghuraman Mudumbai, Joao Hespanha, Upamanyu Madhow, and Gwen Barriac. 2005. Scalable feedback control for distributed beamforming in sensor networks. In *IEEE ISIT*.
- [85] Raghuraman Mudumbai, Ben Wild, Upamanyu Madhow, and Kannan Ramchandran. 2006. Distributed beamforming using 1 bit feedback: from concept to realization. In *IEEE Allerton*.
- [86] Kristoffer Olsson and Sveinn Finnsson. 2017. Exploring LoRa and LoRaWAN. (2017).
- [87] Yao Peng, Longfei Shangguan, Yue Hu, Yujie Qian, Xianshang Lin, Xiaojiang Chen, Dingyi Fang, and Kyle Jamieson. 2018. Plora: A passive long-range data network from ambient lora transmissions. In *ACM SIGCOMM*.
- [88] Ada SY Poon, Stephen O'Driscoll, and Teresa H Meng. 2010. Optimal frequency for wireless power transmission into dispersive tissue. *IEEE Transactions on Antennas and Propagation* (2010).
- [89] Morgan Quigley, Ken Conley, Brian Gerkey, Josh Faust, Tully Foote, Jeremy Leibs, Rob Wheeler, and Andrew Y Ng. 2009. ROS: an open-source Robot Operating System. In *ICRA workshop on open source software*. Kobe.
- [90] Hariharan Shankar Rahul, Swarn Kumar, and Dina Katabi. 2012. JMB: scaling wireless capacity with user demands. In *ACM SIGCOMM*.
- [91] Anil Kumar RamRakhyani and Gianluca Lazzi. 2013. On the design of efficient multi-coil telemetry system for biomedical implants. *IEEE Transactions on Biomedical Circuits and Systems* (2013).
- [92] Anil Kumar RamRakhyani, Shahriar Mirabbasi, and Mu Chiao. 2011. Design and optimization of resonance-based efficient wireless power delivery systems for biomedical implants. *IEEE Transactions on Biomedical Circuits and Systems* (2011).
- [93] G Radha Rani and GSN Raju. 2013. Transmission and reflection characteristics of electromagnetic energy in biological tissues. *International Journal of Electronics and Communication Engineering* (2013).
- [94] Mahdi Rasouli and Louis Soo Jay Phee. 2010. Energy sources and their development for application in medical devices. *Expert review of medical devices* (2010).
- [95] G Enrico Santagati and Tommaso Melodia. 2015. U-wear: Software-defined ultrasonic networking for wearable devices. In *ACM MobiSys*.
- [96] G Enrico Santagati and Tommaso Melodia. 2017. An implantable low-power ultrasonic platform for the Internet of Medical Things. In *IEEE INFOCOM*.
- [97] JC Schuler. 1961. High-level electromagnetic energy transfer through a closed chest wall. *IRE International Conv. Rec. pt 9* (1961).
- [98] Longfei Shangguan and Kyle Jamieson. 2016. The design and implementation of a mobile rfid tag sorting robot. In *ACM MobiSys*.
- [99] Antonietta Stango, Kamya Yekeh Yazdandoost, Francesco Negro, and Dario Farina. 2016. Characterization of in-body to on-body wireless radio frequency link for upper limb prostheses. *PLoS one* (2016).
- [100] A Surowiec, SS Stuchly, L Eidus, and A Swarup. 1987. In vitro dielectric properties of human tissues at radiofrequencies. *Physics in Medicine & Biology* (1987).
- [101] Shin-nosuke Suzuki, Shunsuke Kimura, Tamotsu Katane, Hideo Saotome, Osami Saito, and Kazuhito Kobayashi. 2002. Power and interactive information transmission to implanted medical device using ultrasonic. *Japanese journal of applied physics* (2002).
- [102] Vamsi Talla, Mehrdad Hesar, Bryce Kellogg, Ali Najafi, Joshua R Smith, and Shyamnath Gollakota. 2017. Lora backscatter: Enabling the vision of ubiquitous connectivity. *Proceedings of the ACM on Interactive, Mobile, Wearable and Ubiquitous Technologies* (2017).
- [103] Vamsi Talla, Bryce Kellogg, Benjamin Ransford, Saman Naderiparizi, Shyamnath Gollakota, and Joshua R Smith. 2015. Powering the next billion devices with Wi-Fi. In *ACM CoNext*.
- [104] David Tse and Pramod Viswanath. 2005. *Fundamentals of wireless communication*. Cambridge university press.
- [105] Deepak Vasisht, Guo Zhang, Omid Abari, Hsiao-Ming Lu, Jacob Flanz, and Dina Katabi. 2018. In-body backscatter communication and localization. In *ACM SIGCOMM*.
- [106] Ju Wang, Jie Xiong, Xiaojiang Chen, Hongbo Jiang, Rajesh Krishna Balan, and Dingyi Fang. 2017. TagScan: Simultaneous target imaging and material identification with commodity RFID devices. In *ACM MobiCom*.
- [107] Jingxian Wang, Junbo Zhang, Rajarshi Saha, Haojian Jin, and Swarn Kumar. 2019. Pushing the Range Limits of Commercial Passive RFIDs. In *USENIX NSDI*.
- [108] Chi Zhang, Sidharth Kumar, and Dinesh Bharadia. 2019. Capttery: Scalable Battery-like Room-level Wireless Power. In *ACM MobiSys*.
- [109] Pengyu Zhang, Mohammad Rostami, Pan Hu, and Deepak Ganesan. 2016. Enabling practical backscatter communication for on-body sensors. In *ACM SIGCOMM*.

## APPENDIX

### A $P_{CCS(0)}$ EXTRACTION

Let  $x(t)$ ,  $X(\omega)$ ,  $p(t)$ ,  $P(\omega)$ ,  $n(t)$ , and  $N(\omega)$  be the reference chirp symbol, received backscatter signal, and channel noise in the time domain and frequency domain, respectively. When the leader radio detects the backscatter signal, it multiplies incoming signals with the complex-conjugate copy of the reference chirp:  $(p(t)+n(t))x^*(t)$ . Next we prove  $P_{CCS(0)}$  is the peak value of  $(p(t)+n(t))x^*(t)$ , and it changes monotonically with the strength of backscatter input signal  $p(t)$ .

Recall that multiplication in time domain is equivalent to the convolution in the frequency domain, we can rewrite the former expression as:

$$x^*(t)(p(t)+n(t)) = X^*(-\omega) * P(\omega) + X^*(-\omega) * N(\omega) \quad (1)$$

On the other hand, the cross-correlation can be represented as  $X(\omega) \otimes P(\omega) = X(-\omega) * P(\omega)$  [14]. Hence we can rewrite above expression as:

$$x^*(t)(p(t)+n(t)) = X(\omega) \otimes P(\omega) + X(\omega) \otimes N(\omega) \quad (2)$$

where  $X(\omega) \otimes N(\omega)$  is a constant noise term,  $X(\omega) \otimes P(\omega)$  is the cross-correlation between the reference chirp and the backscatter signal, and  $\omega$  is the cross-correlation lag. When In-N-Out detects the incoming backscatter signal, it synchronizes the reference chirp with this backscatter signal by shifting the reference chirp at the frequency domain. This operation leads to a cross-correlation peak (if there is a peak) shows at the zero lag position. Without loss of generality, we neglect the noise term of the above expression and use  $P_{CCS(\omega)}$  to represent the frequency domain cross-correlation

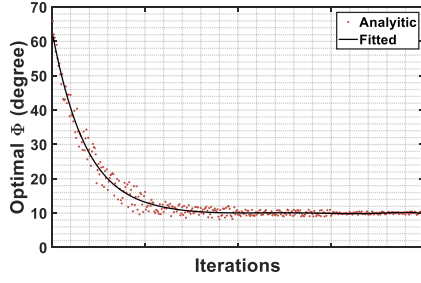


**Figure 29: Optimal phase searching bond and its corresponding 7 order polynomial fitting curve in the context of backscatter assisted beamforming.**

between the incoming backscatter signal and the reference chirp.

$$\begin{aligned}
 P_{CCS(\omega)} &= X(\omega) \otimes P(\omega) \\
 &= \frac{1}{2\pi} \int_0^{2\pi} \left( \sum_{m=-\infty}^{\infty} x(-m)e^{i\sigma m} \right) \left( \sum_{k=-\infty}^{\infty} p(k)e^{-i(\omega-\sigma)k} \right) d\sigma \\
 &= \sum_{m=-\infty}^{\infty} x(-m) \sum_{k=-\infty}^{\infty} p(k)e^{-i\omega k} \frac{1}{2\pi} \int_0^{2\pi} (e^{-i\sigma(-m-k)}) d\sigma \\
 &= \sum_{m=-\infty}^{\infty} x(-m) \sum_{k=-\infty}^{\infty} p(k)e^{-i\omega k}.
 \end{aligned} \tag{3}$$

Hence the  $P_{CCS(0)}$  (zero lag peak strength) can be expressed as:

$$P_{CCS(0)} = \sum_{m=-\infty}^{\infty} x(-m)p(m) \tag{4}$$

The above expression indicates that  $P_{CCS(0)}$  is *linearly proportional* to the power of backscatter signal  $p(\cdot)$ . The leader radio thus adopts the power change of  $P_{CCS(0)}$  as the indicator of the power change received at the backscatter.

## B OPTIMAL PHASE SEARCHING BOUND ESTIMATION

According to the Proposition 3 in [83], the expected value of the beamforming amplitude after  $n^{th}$  period is:

$$y[n+1] = y[n](1 - p(1 - C_{\Phi})) + \frac{\sigma_1}{\sqrt{2\pi}} e^{-\frac{(y[n](1-C_{\Phi}))^2}{2\sigma_1}}. \tag{5}$$

where

$$\begin{aligned}
 p &= Q\left(\frac{y[n](1 - C_{\Phi})}{\sigma_1}\right), \\
 \sigma_1^2 &= \frac{N}{2} \left( (1 - C_{\Phi}^2) - \frac{I_2(\eta_n)}{I_0(\eta_n)} (C_{\Phi}^2 - C_{2\Phi}) \right), \\
 C_{\Phi} &\doteq E_{\Phi}(\cos\Phi_i), \\
 I_k(x) &= \frac{1}{2\pi} \int_{-\pi}^{\pi} \cos(k\phi) e^{x\cos(\phi)} d\phi.
 \end{aligned} \tag{6}$$

where  $I_k(x)$  is the modified first-kind,  $n$ -order Bessel function,  $\eta_n$  is characterized by  $\frac{I_1(\eta_n)}{I_0(\eta_n)} = \frac{y[n]}{N}$ .  $Q(\cdot)$  is the tail distribution function of the standard normal distribution.

In the context of the backscatter assisted beamforming system. We first measure the backscatter signal power at different carrier

signal power settings. These results are then fitted using a nonlinear function, which is denoted by  $P_o = \varphi(P_i)$ . Combining this nonlinear function with Equation 5, we have:

$$y[n+1] = \varphi(y[n](1 - p(1 - C_{\Phi})) + \frac{\sigma_1}{\sqrt{2\pi}} e^{-\frac{(y[n](1-C_{\Phi}))^2}{2\sigma_1}}). \tag{7}$$

At each time slot  $n$ , we can calculate the optimal distribution of phase searching bound  $g_n(\Phi_i)$  by solving the following optimization problem:

$$\arg \max_{g_n(\Phi_i)} (y[n+1] - y[n]) \tag{8}$$

The problem of choosing an optimal distribution of phase searching bound is equivalent to the problem of finding the optimal variation of the phase searching bound. Given the fitted power function  $P_o = \varphi(P_i)$ , We compute the optimal phase searching bond at each iterations and plot the result in Figure 29. To minimize the jitters, we then fit this analytical result using a high order nonlinear polynomial curve function  $\Phi = P(n)$ . This function is then employed for setting the phase searching bound in each beamforming iteration.